Ultrastrong, Highly Conductive and Capacitive Hydrogel Electrode for Electron-ion Transduction

Bowen Yao
University of California Los Angeles

Yichen Yan
University of California Los Angeles

Quincy Cui
University of California Los Angeles

Sidi Duan
University of California Los Angeles

Canran Wang
University of California Los Angeles

Yingjie Du
University of California Los Angeles

Yusen Zhao
University of California Los Angeles

Dong Wu
University of California Los Angeles

Shuwang Wu
University of California Los Angeles

Xinyuan Zhu
Shanghai Jiao Tong University

Tzung Hsiai
University of California Los Angeles

Ximin He (✉ ximinhe@ucla.edu)
University of California Los Angeles   https://orcid.org/0000-0001-8845-4637

Article

Keywords:

1   **Ultrastrong, Highly Conductive and Capacitive Hydrogel Electrode for Electron-ion**
2   **Transduction**

3   **Authors:**   Bowen Yao[1,2†], Yichen Yan[1†], Quincy Cui[3], Sidi Duan[1], Canran Wang[1], Yingjie Du[1],
4   Yusen Zhao[1], Dong Wu[1], Shuwang, Wu[1,2], Xinyuan Zhu[2], Tzung Hsiai[3], Ximin He[1*]
5   **Affiliations:** [1]Department of Materials Science and Engineering, University of California, Los
6   Angeles, CA 90095.
7   [2]School of Chemistry and Chemical Engineering, State Key Laboratory of Metal Matrix
8   Composites, Shanghai Jiao Tong University, Shanghai 200240, China.
9   [3]Department of Bioengineering, University of California, Los Angeles, CA 90095.
10   [†]These authors contributed equally to this work.
11   [*] E-mail: ximinhe@ucla.edu

12

13   **Abstract**

14   Electron-ion transduction is the cornerstone for electronic devices interfacing with biological
15   organisms and promoting emerging ionotronic devices, ranging from basic electronic elements
16   to wearable electronics and energy harvesting devices. However, with commonly used metal
17   electrodes, the electron-ion transduction suffers from high impedance, signal distortion and
18   poor voltage tolerance. Surface modification with conductive porous materials could partially
19   remedy these issues but is inevitably accompanied by weak interfacial adhesion and
20   mechanical weakness. Therefore, freestanding electrodes integrating high mechanical and
21   electrical properties are highly demanded. Herein, a general strategy is discovered to ameliorate
22   these issues by introducing a conducting polymer (CP) hydrogel electrode of ultrahigh strength
23   (~30 MPa) and conductivity (up to ~1200 S cm^{-1}) with a capacitive behavior. These features
24   are derived from the conductive nanoporous matrix with π-π interactions as both crosslinking
25   sites and electron-transfer pathways, through surface gelation coupled with secondary-doping
26   and densification. This strategy significantly decreased the low-frequency impedance and
27   improved the signal fidelity, without affecting its high-frequency response. Furthermore,
28   excellent biocompatibility, multifunctionality, and heart pacing upon ultra-low voltage (60%
29   reduction) have also been demonstrated, showing the great potential of this CP material for
30   bioelectronic applications and various human-machine interfaces.

31

32

33

Introduction

While living organisms transmit signals via ions[1], conventional manmade electronic devices mostly rely on electron transport. To bridge the electronic realm and the biological world, two promising technologies – bioelectronics and ionotronics – have emerged, attempting to transduce electronic and ionic signals in both directions. For example, bioelectronics is developed to detect electrophysiological signals derived from the ionic concentration gradience across cell membranes, including electrocardiogram (ECG) for the diagnosis of heart disease[2], electroencephalography (EEG) for brain-computer interface[3]. Reversely, bioelectronics can also deliver ions into bio-tissues for medical therapy[4, 5], typically in electrical stimulation as brain, heart, or muscle disease therapies[6, 7]. Meanwhile, ionotronic devices are being developed to be next-generation electronics, which are usually constructed using hydrogels and elastomers and function with a hybrid circuit of mobile ions and mobile electrons. They are expected to open up numerous unprecedented opportunities in energy harvesting (triboelectricity[8], ionic concentration gradient[9, 10] or thermo-gradient generator[11]) and a series of stretchable/soft analogs of conventional electronics, such as flexible transistors[12], logic circuits[13], displays[14] and soft robots[15, 16].

Inert metals were often employed as the electrodes of current bioelectronics and ionotronics to transduce electronic and ionic signals[17, 18]. However, they have several issues, including: (i) a high and unstable impedance across the electrode/electrolyte interface, causing a significant loss and distortion of low-frequency signals (< 100 Hz), which are highly important in many applications, such as low-grade energy conversion (*e.g.*, low-frequency vibration of < 5 Hz)[8], electromechanical transduction (*e.g.*, actuators working at 0.01-100 Hz)[19], electrophysiological recordings (*e.g.*, neural local-field potential, typically < 100 Hz)[20]; (ii) a high voltage drop across the electrode/electrolyte interface, due to the high impedance upon low frequency, inducing undesirable faradic electrochemical reactions. One strategy to remedy this issue is introducing a faradic process to the electrode (*e.g.*, Ag/AgCl), through which electrochemical reaction current passes. However, it suffers from low interfacial stability, mutable electrode potential, and potential toxicity, caused by the Ag^+ released for long-term implantation[21, 22].

An alternative to employing electrochemical reactions is modifying the inert metal electrodes with conductive porous materials, such as porous carbon materials. With the

65 increased electrical-double-layer (EDL) capacitance, the interfacial impedance could be
66 decreased[7]. Although EDL-capacitive materials have been heavily developed to pursue a
67 maximum charge storage ability for energy storage applications, their mechanical strength and
68 conductivity were severely compromised, unbeneficial for the interfacial stability and
69 robustness for bio-/iono-electronics. For example, porous graphene[23, 24] or metal-oxide
70 frameworks (MOF)[25] with high EDL capacitances usually have poor mechanical properties
71 (*e.g.,* powder state for MOF) and/or low conductivities ($1-100$ S cm^{-1}); poly(3,4-
72 ethylenedioxythiophene):polystyrene sulfonate (PEDOT:PSS) hydrogels could possess both
73 good EDL capacitance and good conductivity, but usually have a low mechanical strength (*e.g.,*
74 0.1-2 MPa)[26-29]. The intrinsic conflict among capacitance, conductivity and mechanical
75 properties severely limits the molecular design of electrode materials, as a large capacitance
76 requires high porosity which inevitably impairs the electrical conductance pathway and
77 structural integrity. Additionally, using rigid inert metals as the current collectors has been
78 found to induce adverse immune responses at the implantation sites, due to the mechanical
79 mismatch between the electronic materials and organisms (*e.g.,* shear-induced inflammation
80 and the consequent formation of glial scar)[30].

81   It is worth noting that, rather than a high energy storage capability, the high fidelity of
82 electron-ion interconversion independent of voltage and frequency is the core for bio/iono-
83 electronics but this vital issue has not been addressed[4]. Therefore, based on our electrical model
84 and analysis (see *Supplementary Discussion Section 1*), the ideal electrode material for bio-
85 /iono-electronics should have simultaneously three key features: an EDL capacitance behavior
86 (without electrochemical reactions), a high electrical conductivity (alleviating the need for
87 metal current collectors) and good mechanical properties (strong and flexible), along with high
88 stability and good biocompatibility.

89 Forming EDL requires a conductive matrix with a large specific surface area, while both
90 efficient electron transfer and improved mechanical strength require a high continuity with
91 strong molecular interaction. Thus, we propose that a polymer network with interconnected
92 nano-sized pores and dense pore walls in a continuous, highly-oriented network would be an
93 ideal structure for the electrode material that integrates high mechanical strength and high
94 electrical conductivity with a capacitive behavior. Herein, we have developed a new strategy,
95 surface gelation coupled with secondary doping and partial densification, to create conducting

96 polymer (CP) hydrogels with such a desirable complex nanostructure. Based on PEDOT:PSS

97 as an exemplary model material in this work, our CP hydrogels are ultra-strong (up to ~30 MPa

98 fracture strength), highly conductive (up to ~1,200 S cm^{-1}) and capacitive (see *Supplementary*

99 *Tables S1 and S2* for detailed comparisons), and thus capable of serving as a freestanding

100 electrode to convert ion-electron signals without involving metal current collectors (Fig. 1a).

101
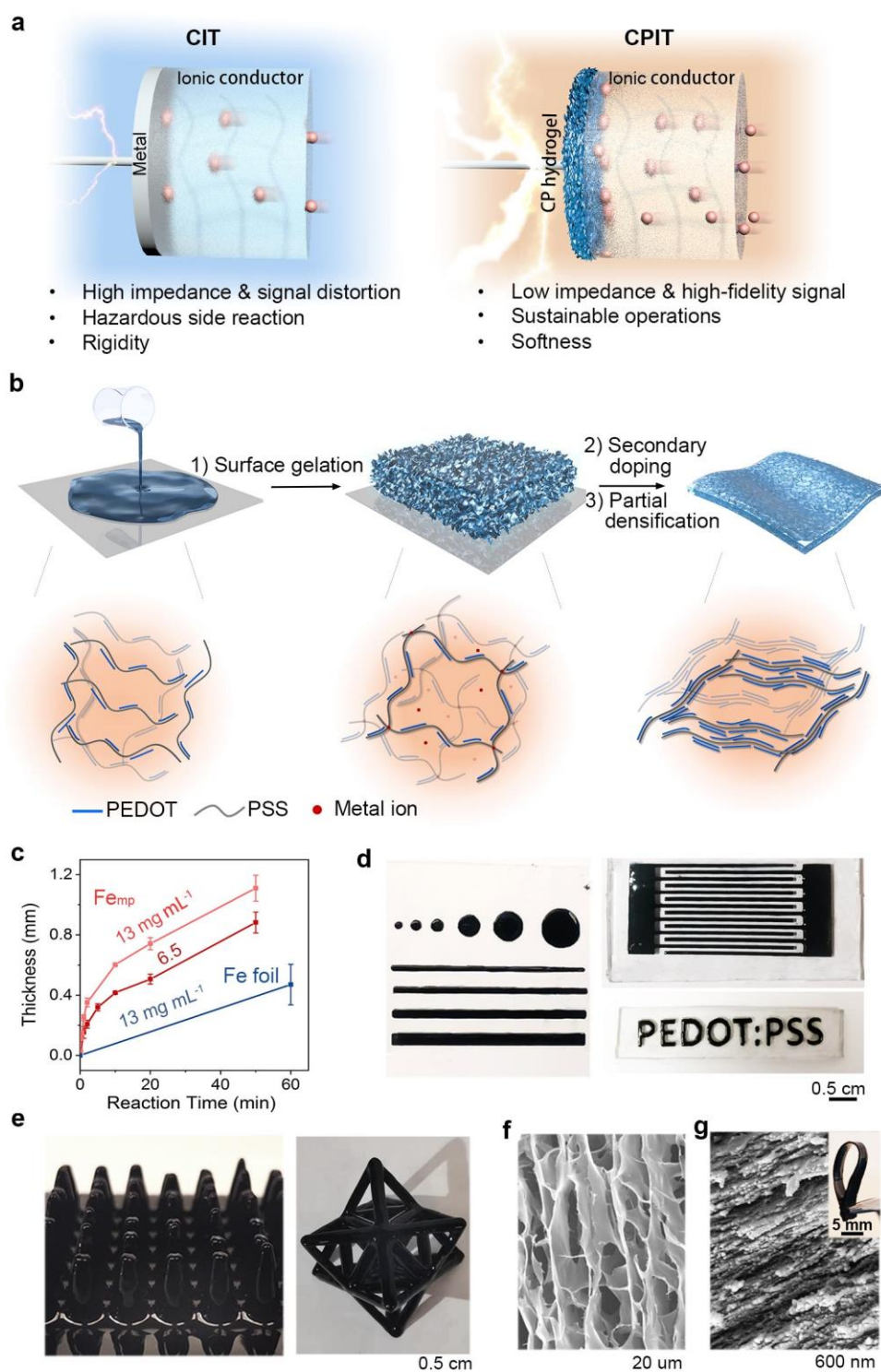
102 **Fig. 1| Schematics of ionotronics and preparations of conducting polymer (CP) hydrogel. a,** Illustrative
103 schematics of common ionotronics (CIT) with metal as the electrode and conducting-polymer-assisted
104 ionotronics (CPIT) with PEDOT:PSS hydrogel as the electrode. Compared with CIT, CPIT has a lower
105 interfacial impedance (electrode/electrolyte interface), a lower interfacial voltage for more sustainable
106 operations and a more stable signal transmission ability. **b,** Preparation procedure of CP hydrogels with the
107 corresponding structural change of CP chains. The upper panel: CP suspension was applied onto the surface
108 PDMS substrate coated with Fe-microparticle (Fe_{mp}) and kept still for 12 h for interfacial gelation. Then, a
109 freestanding CP hydrogel film was obtained after secondary doping and partial densification. The lower
110 panel illustrates the transformation of molecular structures of CPs: the CP chains were crosslinked by iron
111 ions that were produced through the in-situ corrosion of Fe powder by acidic PSS chains. Then, after
112 secondary doping and partial densification, the CP chains underwent a configurational transformation to a
113 laminar structure with a high crystalline degree. **c,** Gelation kinetics of the CP suspension on the Fe_{mp}-coated
114 PDMS or Fe foil. Before acid treatment, the thicknesses of the CP hydrogels, prepared by dropping 13 or
115 6.5 mg mL^{-1} CP suspension on Fe-powder-coated PDMS substrate or Fe foil, were plotted against the
116 reaction time. **d, e,** Photographs of CP suspension selectively gelating on the patterned Fe_{mp}-coated 2D
117 PDMS substrate (**d**), 3D PDMS conical pillar array (left in the panel **e**), and 3D epoxy lattice structure (right
118 in the panel **e**). **f, g,** SEM images of freeze-dried CP hydrogel before (**f**) and after (**g**) secondary doping.

119   With these desirable properties, CP–based ionotronics (CPITs) were fabricated to
120 demonstrate their ability of effectively solving the electron-ion transduction issues. By
121 employing the CP hydrogel electrodes, the transduction fidelity was greatly improved with
122 enhanced frequency-independency and voltage-tolerance, through a drastic decrease of the
123 low-frequency impedance at the electrode/ionic-conductor interfaces by nearly two orders of
124 magnitude. Therefore, this strategy may be expected to significantly enhance the performance
125 of various ionotronic devices, including ionic transistors, ionic-driven electric generators and
126 ionic-based bioelectronics. Finally, besides the application in ionotronics, the benefits of CP
127 hydrogel electrodes in bioelectronics were also demonstrated by electrical stimulation
128 promoted cell proliferation and excellent porcine heart pacing with 75% pacing voltage
129 threshold reduction compared to commercial electrodes, further highlighting the strong ion-
130 injection ability.

131

132 **Preparation of PEDOT:PSS hydrogels**
133   The PEDOT:PSS-based CP hydrogel film was synthesized by crosslinking a commercially
134 available CP suspension on a polydimethylsiloxane (PDMS) substrate coated with a 1-3 μm
135 thin layer of carbonyl Fe microparticle (Fe_{mp}) (Fig. 1b, c). The surface gelation mechanism is

136 based on the decreased electrostatic repulsion between the negative-charged PEDOT:PSS

137 chains, promoted by the positive-charged iron ions which are uniquely *in-situ* produced through

138 the corrosion of Fe_{mp} by the acidic PSS upon deposition (See *Supplementary Discussion*

139 *Section 2* for detailed mechanism and kinetics studies).

140 To demonstrate the attractive convenience and versatility of this surface gelation method,

141 CP hydrogels of various 2D patterns (dot, line, bird, letters, and interdigitation) with a 150 μm

142 resolution were fabricated on Fe_{mp}-coated PDMS simply with shadow masks (Fig. 1d,

143 Supplementary Figs. S2-S4); CP hydrogels grown on the surfaces of complex 3D structures,

144 including lattice, curved surface and needle array, were also constructed (Fig. 1e). Moreover,

145 bulk hydrogels with substantial thicknesses at centimeter-scale could also be prepared,

146 attributed to the good diffusion of metal ions. The entire fabrication could be completed under

147 an ambient condition by employing different active metals besides Fe_{mp} as substrates (*e.g.,* Fe,

148 Zn, Sn, and Al foils) with all off-the-shelf chemicals (Supplementary Figs. S5, S6),

149 demonstrating the easy preparation of the CP hydrogels and potential for large-scale production.

150 Overall, the surface gelation has a good thickness controllability and benefits conformal

151 coating on various substrates of arbitrary geometries, 2D patterning and 3D printability.

152 Additionally, the resulting CP network contained a large number of nanopores and restricted

153 the excessive stacking of CP building blocks in the following secondary doping and partial

154 densification steps, thus beneficial to the EDL formation.

155 Yet, these as-prepared PEDOT:PSS hydrogels (CP_{ap}) with electrostatic attraction-based

156 crosslinking are mechanically weak and possess low conductivity (< 1 S cm^{-1}), not satisfying

157 the requirements of serving as the electrodes. Fortunately, their electrical and mechanical

158 properties could be greatly improved with a secondary doping method via phase separation and

159 configurational transformation mechanisms[42]. Here, H_2SO_4 was used as a treating agent due to

160 its inexpensiveness and outstanding performance (See *Supplementary Discussion Section 3* for

161 detailed mechanism studies). Subsequently, the pore structure, another important parameter

162 influencing the properties of PEDOT:PSS hydrogel, was also carefully tuned by a 'controlled

163 densification' strategy, where the hydrogels were infiltrated with a diluted H_2SO_4 aqueous

164 solution, dried and then dialyzed in sequence. During this process, the water evaporation drove

165 the shrinkage of micropores into nanopores and also a decrease in the hydrogel membrane

166 thickness, while the majority of original nanopores were well retained (*Supplementary Fig.*

167 *S11*). The degree of such structure modifications could be controlled by the water concentration

in the H₂SO₄ solutions. Overall, as a result, the large number of nanopores enabled a high volumetric capacitance, and the densified polymer network (pore wall) effectively further improved the mechanical strength and conductivity, owing to the increased crosslinking densities through more and stronger π-π interactions and interconnection of the conductive PEDOT-rich domains. Additionally, with the stronger interaction of PEDOT:PSS chains, the hydrogel could maintain the micro-/nano-morphology without swelling when soaking in purified water or physiological saline, which endowed the material excellent structural stability.
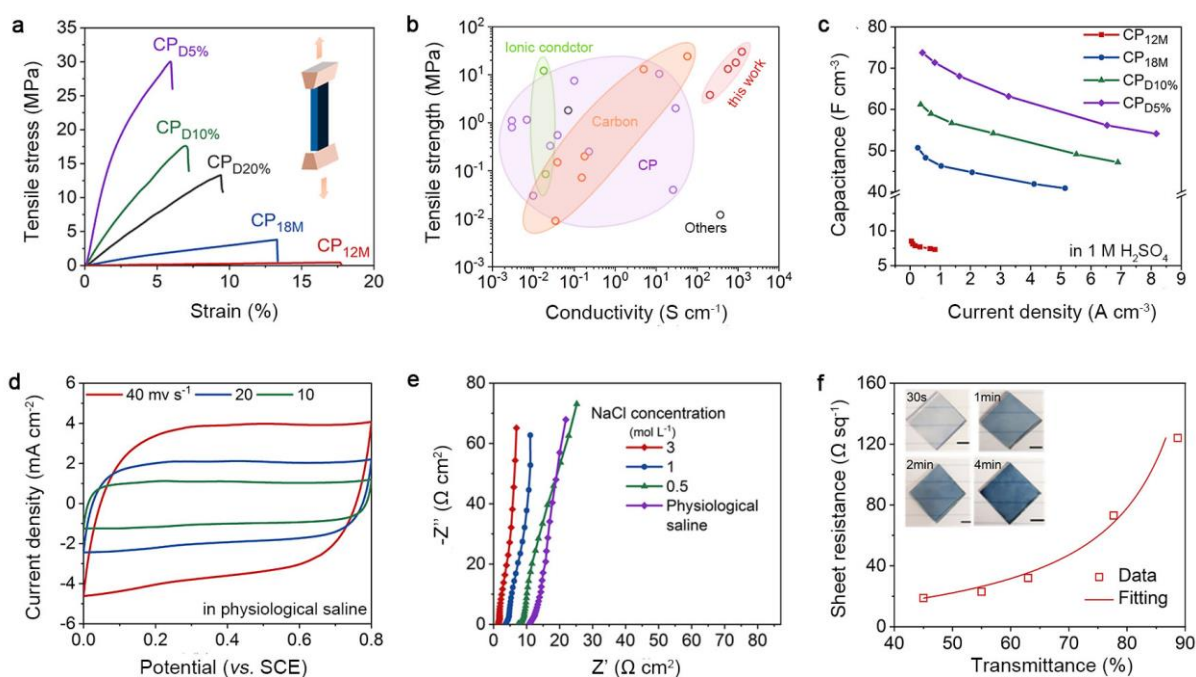
Fig. 2| Properties of the PEDOT:PSS (CP) hydrogels. a, Tensile stress-strain curves of freestanding CP hydrogels at the strain rate of 100 % min⁻¹. **b,** An Ashby-style plot comparing the conductivity and strength of the CP hydrogels with the values of previously reported conductive hydrogels (including CP-based, carbon-based or ionic-conductive hydrogels) (data points are from references mentioned in Supplementary Fig. S12 and Supplementary Table S2). **c,** Comparisons of the volumetric specific capacitance of CP hydrogels in 1 M H₂SO₄ electrolyte., calculated from GCD curves (Supplementary Fig. S13-16). **d,** CVs of CP₁₈ₘ hydrogel (thickness = 24 μm) at different scan rates and current densities in physiological saline by using a three-electrode setup. **e,** The Nyquist plot of CP₁₈ₘ hydrogel, tested in a three-electrode setup with physiological saline as the electrolyte, at a frequency range of ~10⁵-0.026 Hz. **f,** Sheet-resistance vs. transmittance curve of semi-transparent CP hydrogel membrane on PDMS substrate. Insets are the optical image of CP hydrogel membrane prepared through interfacial gelation for different time (0.5, 1, 2, and 4 min) followed by acid treatment and dialysis. Scale bar = 0.5 cm.

190   Using the above method, a series of acid-treated PEDOT:PSS hydrogels with tunable
191   mechanical and electrical properties for different practical applications, including hydrogels
192   only underwent secondary doping process with 12 M or 18 M H_2SO_4 (namely CP_{12M} or CP_{18M})
193   treatment, and dense hydrogels prepared from CP_{18M} followed by controllable densification,
194   by employing 20%, 10% and 5% (v_{acid}/v_{water}) H_2SO_4 solutions as densifying agents respectively
195   (namely $CP_{D20\%}$, $CP_{D10\%}$, and $CP_{D5\%}$).

196

197   **Mechanical and electrical properties**

198   Taking full advantage of regulatable composition, configuration, crystallinity, and micro-
199   /nano-porous morphology by secondary doping and partial densification, CP hydrogel films
200   with tunable mechanical properties were therefore obtained. They showed excellently high
201   fractural strength, which increased with the H_2SO_4 concentration (in the secondary doping
202   process) and the densification degree of hydrogel, much higher than those of conductive
203   hydrogels reported previously (Fig. 2a, 2b and Supplementary Fig. S12)[28, 29, 31]. We believe
204   this was caused by the high-degree crystallization of PEDOT chains, stronger molecular
205   interaction and denser laminar structure, which were verified by the morphology and structural
206   characterizations (See *Supplementary Discussion Section 3*)[26, 32]. In detail, the $CP_{D5\%}$ displayed
207   the highest tensile strength (~30 MPa) with the shortest fracture strain (~5.9%), providing
208   outstanding structural stability for soft electronics. The CP_{12M} possessed the lowest tensile
209   strength of ~0.42 MPa with the largest fracture strain of ~17%. The conductivity of the CP
210   hydrogels also displayed a positive relationship with H_2SO_4 concentration (in the secondary
211   doping process) and densification degree, increasing from 143 S cm^{-1} for CP_{12M} to 1254 S cm^{-1}
212   for $CP_{D5\%}$, which are $10\sim10^3$ higher than the conductivities of previously reported CP
213   hydrogels with similar solid contents (Fig. 2b).

214   Whiling having these excellent mechanical properties and conductivity, the PEDOT:PSS
215   hydrogels also showed a nearly ideal EDL capacitance, large enough for efficient electron-ion
216   transduction when serving as both electrodes and conductors. For comparison, other porous
217   materials explored for supercapacitors or batteries before usually suffered from either low
218   conductance or low mechanical strength (Supplementary Table S1 for detailed comparison).
219   For example, porous reduced graphene oxide showed a conductivity of only 30 S cm^{-1};
220   conductive MOF with EDL capacitance was usually in a powder form. To compare the intrinsic
221   electrochemical properties of CP hydrogels, highly ionically conductive 1 M H_2SO_4 electrolyte

222 solution was used as an electrolyte at the beginning, the cyclic voltammetry (CV) curves of all

223 CP hydrogel films showed a quasi-rectangular shape and a linear relationship between current

224 and scan rates ranging from 10 to 400 mV s^{-1} (Supplementary Figs. S13-S16). According to

225 the galvanostatic charge-discharge tests (GCD) and EIS (Fig. 2c, *Supplementary Discussion*

226 *Section 4.1*), the CP$_{12M}$ showed the highest areal capacitance (128 mF cm^{-2} at 0.62 mA cm^{-2})

227 with the lowest volumetric capacitance (8.5 F cm^{-3} at 0.41 A cm^{-3}) among all the PEDOT:PSS

228 hydrogels due to the presence of micron-pores. In contrast, CP$_{D5\%}$ showed a similar areal

229 capacitance (109 mF cm^{-2} at 0.62 mA cm^{-2}) but a significantly high volumetric capacitance

230 (73.7 F cm^{-3} at 0.41 A cm^{-3}) brought by its dense micro-morphology (Supplementary Figs.

231 S13-S18). These results indicate the majority of nanopores responsible for the EDL formation

232 were successfully retained after secondary doping and partial densification process.

233 Interestingly, CP hydrogel could still show capacitive behavior with a similar capacitance

234 (~110 mF cm^{-2} at 0.62 mA cm^{-2}) in NaCl solution, such as physiological saline, as proved by

235 the CV, GCD and EIS tests (Fig. 2d, 2e, Supplementary Fig. S19-24 and Supplementary

236 Discussion Section 4.2). The good performance in the low NaCl concentrations probably was

237 attributed to the PSS chains acting as polymer electrolytes to provide more ions for the

238 formation of EDLs, showing attractive merit for its applications in physiological environments

239 (*e.g.*, as bioelectronics devices for biological interface engineering).

240 Additionally, by taking advantage of the easy processability of surface gelation, optically

241 transparent or semi-transparent conductive PEDOT:PSS hydrogels with thickness < 100 nm

242 were also fabricated by conducting interfacial gelating in a diluted CP suspension. They

243 showed an increased sheet resistance with transmittance increase, fitting well with the

244 theoretical equation (Fig. 2f, Supplementary Fig. S25, See Methods for details). Additionally,

245 electrochemical impedance tests indicated the phase angles were near 0$^{\mathrm{o}}$ within the input

246 frequencies of 10^5~1 Hz, revealing its electronically conductive characteristics rather than ionic

247 conductance (Supplementary Fig. S25).

248 **The impedance of ionotronics**

249 Considering its high conductivity and capacitance with good mechanical properties, CP$_{18M}$

250 hydrogel, as an example, was then employed as both current collector and electrode to remedy

251
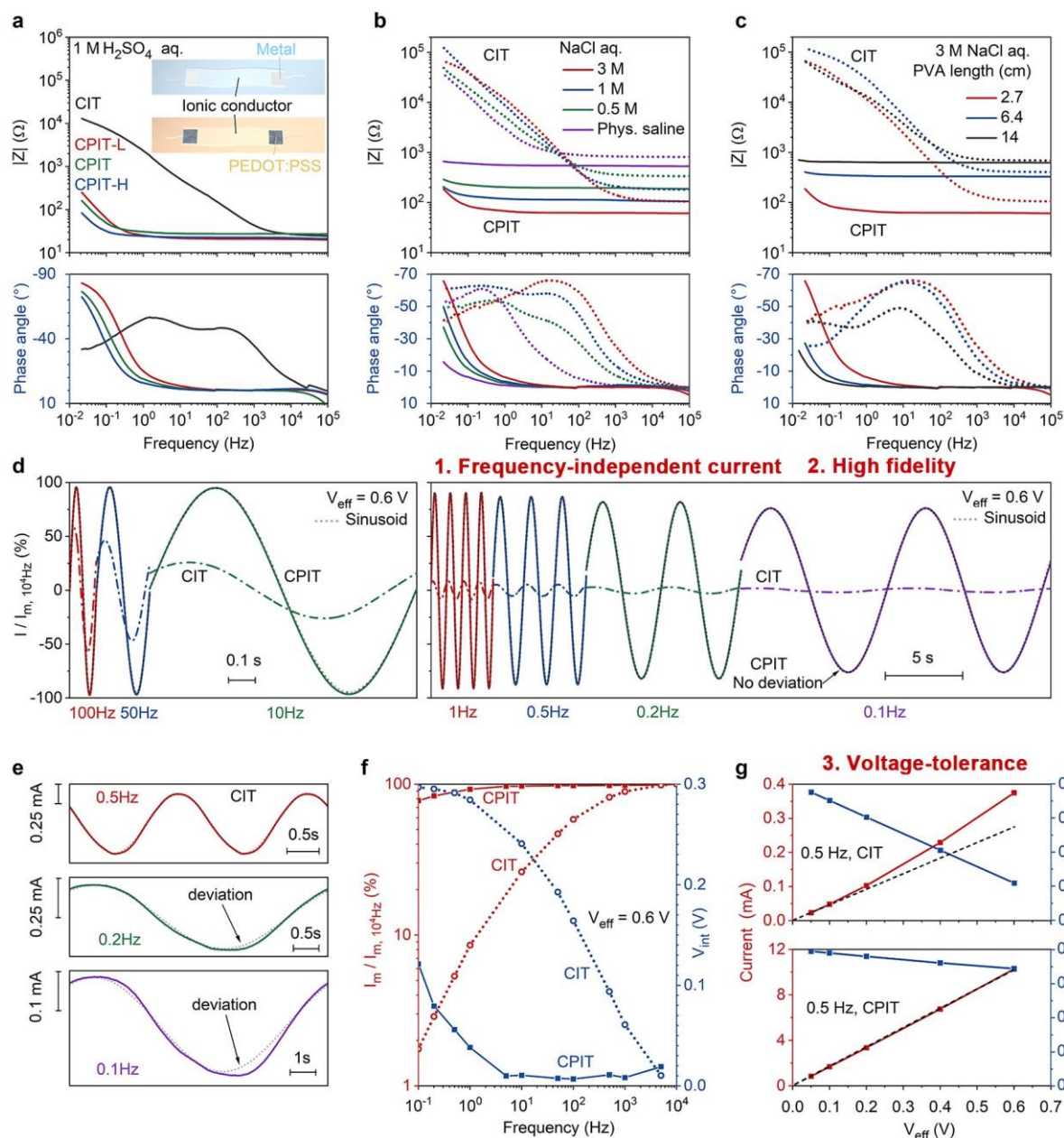
Fig. 3| Electrical properties of common ionotronics (CIT) and conducting polymer-assisted ionotronics (CPIT). a-c, Bode plots (upper: impedance; lower: phase) of CITs and CPITs with PVA-based ionic conductor, where the CIT counterpart was prepared in the same way as the corresponding CPIT but with Pt plates as current collectors: **a,** Current collector: CP_{18M} hydrogels of a high, medium and low areal mass loading (CPIT-H, CPIT, CPIT-L, areal capacitance = 250, 120, 89 mF cm^{-2} at 0.62 mA cm^{-2}, respectively); Electrolyte: 1 M H_2SO_4 solution; insets: schematics of CIT (upper) and CPIT (lower). **b,** Electrolyte: 0.154, 0.5, 1 and 3 M NaCl solutions; Current collector: CP_{18M} hydrogels of a medium mass loading. **c,** Ionic conductor: PVA hydrogels of different lengths; Current collector: CP_{18M} of a medium mass loading. **d,** Normalized current *vs.* time curves of CITs and CPITs upon sinusoidal AC voltage with the efficient voltage (V_{eff}) of 0.6 V. For comparison, the currents were normalized with respect to the maximum value of current

passing through the CIT or CPIT at the AC voltage of 10^4 Hz. The solid and dashed lines are the normalized current of CPITs and CITs, respectively. The gray dotted lines are fitted sinusoids to clarify the deviation of current-time curves from the sinusoidal waveform. **e,** The enlarged current-times curves of CITs in **d** at low-frequency voltage. **f,** Comparisons of the normalized current (red) and the interfacial voltage (blue) of CITs (dotted lines) and CPITs (solid lines) upon sinusoidal voltage input of different frequencies. **g,** Plots of the current (red) and interfacial voltage (blue) *vs.* V_{eff} applied to the CITs and CPITs, upon an input sinusoidal voltage of 0.5 Hz.

the interfacial issues by reducing the impedance of the electrode/electrolyte interface. First, for comparisons, a CIT (control) was fabricated by infiltrating poly(vinyl alcohol) (PVA) hydrogel with 1 M H_2SO_4, which was then attached to two inactive metal (Pt) plates as the electrodes to connect with external circuits (inset in Fig. 3a). According to the Bode impedance plots (Fig. 3a), the CIT showed a low impedance of ~24 Ω with a phase angle of $0.5°$ upon AC voltage of 10^5 Hz, corresponding to the electrolyte resistance of hydrogel (~20 S m^{-1}). However, upon the decrease of the alternating signal frequency, the impedance of the CIT saw a quasi-linear rise and finally reached as high as 10^4 Ω, almost 1000 times higher than the value at 10^5 Hz. Such a high impedance at low frequencies could be mainly attributed to the high impedance of the metal/hydrogel interface. Moreover, in the phase-angle vs. frequency curve (Fig. 3a), upon the decrease of AC frequency, the CIT showed two obvious shoulder peaks at ~100 and 1 Hz respectively, with a serious decrease of phase angle when the frequency further decreased to 0.1 Hz, revealing several faradic processes initiated within the metal/hydrogel interface through chemical reactions (possibly derived from the decomposition of electrolyte and/or oxygen reduction reaction). This extremely complex and uncontrolled electrochemical process would severely impact the signal transduction, and possibly cause interfacial instability of the ionic conductor. Overall, the overly high impedance and non-negligible faradic process severely limit the usages of stretchable and transparent ionotronics in the low-frequency-related applications, in the terms of frequency dependence, interfacial stability and electric signal processing.

Alternatively, by replacing the Pt electrode with the CP_{18M} hydrogel (areal capacitance: ~120 mF cm^{-2}) (Fig. 3a, the green line), CPIT showed a CIT-comparable impedance of ~27 Ω upon high-frequency electricity, but its impedance remained stable without significant increment, upon decreasing the frequency from 10^5 to 1 Hz. When the frequency further decreased from 1 to 0.02 Hz, the impedance of EDL gradually dominated and finally reached

295 only ~250 Ω at 0.022 Hz. For comparison, the impedance ratio of CIT to CPIT ($|Z_{CIT}|/|Z_{CPIT}|$)

296 could reach up to 7, 20, 90, and 120 at the AC frequency of 100, 10, 1 and 0.1 Hz, respectively.

297 Besides, the CPIT also showed a stable phase angle of ~0° within a wide frequency region with

298 a regular and stable increment under the low-frequency region of < 1 Hz, beneficial for signal

299 transduction and processing. The influence of the complex faradic process on impedance,

300 present in the CIT system, was almost negligible in the CPIT system. This could be ascribed

301 to the low impedance of CP hydrogel, which increased the overall current and decreased the

302 voltage across the electrode/electrolyte interface to suppress the harmful electrochemical

303 reactions within it. This is consistent with our theoretical analysis (*Supplementary Discussion*

304 *Section 1*).

305 Our proposed CPIT strategy is a general method to ameliorate the low-frequency

306 performance issues for different ionic conductors, which was proved by using CP hydrogel

307 with different areal capacitances (Fig. 3a), and by using different ionic conductors with

308 different sizes or ionic conductivities (See *Supplementary Discussion Section 5* for detailed

309 discussion). For example, similar to the trend observed for the ionotronics with hydrogel

310 infiltrated with H_2SO_4 as ionic conductor, all the CPITs with different NaCl electrolyte

311 concentrations and different types or sizes of hydrogel ionic conductors showed significantly

312 depressed impedance growth at low frequencies with stable phase angles (Fig. 3b, 3c). This

313 allows for taking full advantage of the unique properties of different hydrogels, including

314 softness, stretchability, transparency and biocompatibility, *etc.*, to fabricate ionic conductors

315 of high-performance for different applications.

316

317 **Current-time measurement, voltage response and electrical loading**

318 To intuitively study the conductive properties of CIT and CPIT, the current-time curves

319 were recorded when a sinusoidal AC input voltage (V(t)) was applied ($V(t) = \sqrt{2}V_{eff}\sin(2\pi ft)$,

320 V_{eff} is the efficient voltage, f is the frequency). On the whole, the evolved current showed a

321 sinusoidal waveform with a phase difference (φ_V-φ_I) dependent on the EDL capacitance and

322 ionic diffusion resistance of the ionic conductor.
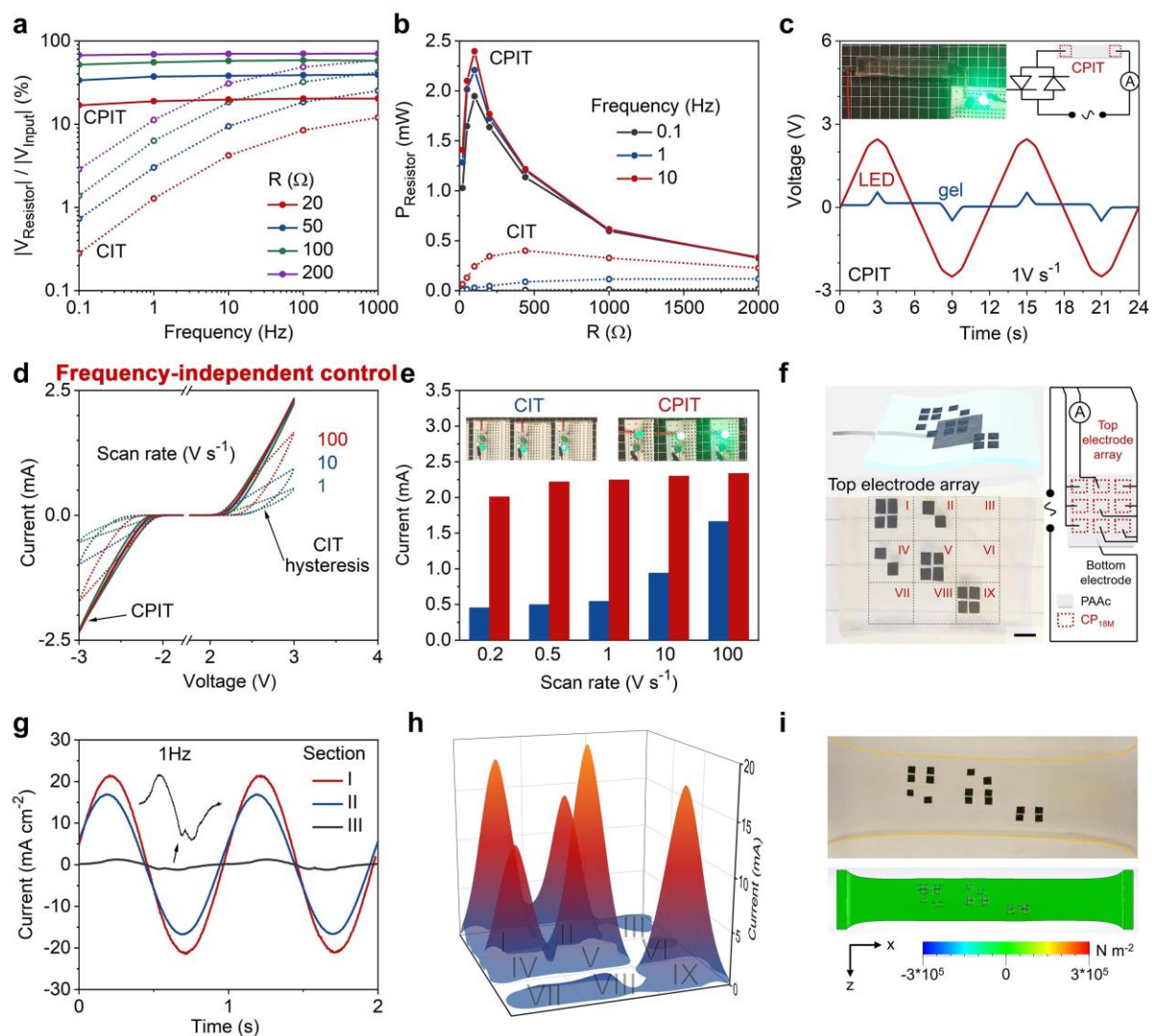
Fig. 4| Demonstrations of the CPIT performance and functions. a, b, Demonstration of CPITs and CITs as ionotronics connected with resistors as electric loadings: **a,** Voltage ratios of resistors to the peak value of input voltage ($|V_{input}| = 0.848$ V) at different frequencies. **b,** the output power of the resistors upon AC voltage of different frequencies. **c-e,** Demonstration of CPITs and CIT as ionotronics connected with LEDs as electric loadings: two LEDs in parallel with reversed polarity were connected to an AC power source with a triangular waveform: **c,** Voltage *vs.* time curves of the CPIT and LEDs. Voltage window: −3~3 V. Sweep rate: 1 V s^{-1}. Insets: an optical image of the setup and relevant circuit diagram. **d,** Cyclic voltammogram of the LED circuit based on CITs (dotted lines) or CPITs (solid lines) as ionotronic devices. Scan rate: 1, 10, and 100 V s^{-1}. **e,** Comparison of the whole current passing through LED circuits under AC voltage of different scan rates. Insets: photos of LEDs during their maximum illumination under the input voltage with different scan rates. **f-i,** Demonstration of an ionotronic device with current density spatial modulation (IC-CDSM): **f,** Schematic diagrams (upper-left) of this ionotronic device where several CP$_{18M}$ hydrogels were attached to one side of an adhesive polyacrylic acid (PAAc) hydrogel as top electrode array, while another CP$_{18M}$ hydrogel on its opposite surface was used as the bottom electrode. The lower-left picture is the digital

338   photography of the top electrode. The lower-right picture is the schematic diagram to depict the current

339   measurement: the electrode array which was divided into 9 domains was connected to an AC power through

340   Pt plate, during which the currents passing through each domain was recorded by a current meter. **g, h,**

341   Electric response of IC-CDSM upon AC voltage. V_{eff}: 0.6 V; Frequency: 1 Hz. **g,** Current *vs.* time curves of

342   the domain I, II, and III on the ionotronic device. Inset: enlarged current profile of domain III. **h,**

343   Comparisons of peak current densities of different domains. **i,** Top: the optical image of the stretched

344   ionotronic device. The boundaries of the PAAc hydrogel were marked with yellow lines for visibility.

345   Bottom: the simulation of the shear stress along x-direction in the xz-plane of the stretched IC-CDSM. Black

346   lines indicate the boundaries of the CP_{18M} and the PAAc hydrogel.

347

348   Upon AC voltage of high frequency (10^4 Hz), the CPMIC and CIT shared a comparable

349   efficient current, corresponding to the electrolyte resistance of the ionic conductor, consistent

350   with their impedance results (Supplementary Fig. S34). When the frequency decreased from

351   10^5 to 0.1 Hz, the current of CIT saw a sharp drop to only 1% of the original value with a phase

352   difference of -60°, while the CPMIC remained 90% of its original current with a phase

353   difference of -20° (Fig. 3d-f, Supplementary S34). Additionally, CIT showed an obvious

354   deviation of the current waveform from sinusoidal shapes especially upon low-frequency AC

355   (Fig. 3e). For comparison, the current waveforms through the CPIT were almost identical to a

356   standard sinusoidal regardless of the input frequencies (Fig. 3d), showing the excellent

357   advantages of CPIT as an ionic conductor to perfectly transmit electric signals with high quality.

358   The high deviation in the CIT circuit could be ascribed to the significant electrochemical

359   reaction initiated by the high voltage across the metal/electrolyte interface with a high

360   impedance upon low-frequency AC (*Supplementary Discussion Section 1*). The interfacial

361   voltage (efficient voltage) can also be directly estimated by vectorially subtracting voltage of

362   electrolyte from input voltage (Fig. 3f, *Supplementary Discussion Section 6*), which were

363   calculated to be only ~0.015 V at 10 Hz and 0.038 V at 1 Hz for CPIT upon an input voltage

364   of 0.6 V. They were much less than those of CIT (~0.24 V at 10 Hz, 0.28 V at 1 Hz), and

365   consistent with our theoretical analysis.

366   Furthermore, to demonstrate the CPIT has a better voltage tolerance than CIT, the effect

367   of the amplitude of AC power voltage was also studied. As expected, as the V_{eff} increased from

368   5 mV to 0.6 V, the output current increased linearly for CPIT with a stable phase angle, but

369   nonlinearly for CIT with an unstable phase angle (Fig. 3g, Supplementary Figs. S35 and S36),

370 ascribed to the acceleration of electrochemical reaction at the metal/electrolyte interface of CIT
371 upon high voltages. This phenomenon was further confirmed by the EIS results, where the CIT
372 saw an obvious decrease in impedance and phase angle at the low-frequency region when the
373 amplitude ranged from 0.05 to 0.6 V (Supplementary Fig. S36). By contrast, with a nearly
374 amplitude-independent impedance and phase angle, the CPIT showed great advantages over
375 CIT in the terms of interfacial stability and electric signal fidelity (Supplementary Fig. S37).

376 To have a better fundamental understanding of the electric response of ionotronics when
377 an electrical appliance was loaded, a theoretical analysis was therefore conducted first. When
378 loaded with a passive appliance (the equivalent circuit is shown in Supplementary Fig. S1), the
379 efficient current ($|\tilde{I}|$) flowing through the circuit and the efficient interfacial voltage ($|\tilde{V}_{EDL}|$)
380 across the hydrogel/electrode interface could be expressed by the following equations:

381
$$|\tilde{I}| = \frac{|\tilde{V}|}{\sqrt{(2R_0 + Z_A{}')^2 + \left(\frac{4}{\omega C_{EDL}} + Z_A{}''\right)^2}} \qquad \text{(Eq. 1)}$$

382
$$|\tilde{V}_{EDL}| = \frac{|\tilde{V}|}{\sqrt{(\omega C_{EDL})^2(2R_0 + Z_A{}')^2 + \left(-4 + \omega C_{EDL} Z_A{}''\right)^2}} \qquad \text{(Eq. 2)}$$

383

384 , where Z_A' and Z_A'' are the real and imaginary impedances of any passive appliance loaded,
385 R_0 and C_{EDL} represent the ionic resistance of hydrogel and EDL capacitance of electrode, and
386 ω is the angular frequency of AC.

387 Upon a low-frequency signal, the induction of the appliance can be neglected (Z_A'' $\leqslant$ 0).
388 Therefore, employing electrodes with a much higher C_{EDL} is thus expected to increase the
389 efficient current and lower the voltage applied to the EDL, beneficial for the voltage tolerance
390 and electrochemical stability of ionotronics. By mathematical approximations, when C_{EDL}
391 increases, the current will increase linearly when the loaded appliance has a much smaller
392 impedance than that of EDL in ionotronics ($4/\omega C_{EDL}$), or the interfacial voltage will decrease
393 inversely to C_{EDL} when a high-impedance appliance is loaded (Supplementary Section 1).

394 Based on this analysis, we experimentally validated the effectiveness of a highly-
395 capacitive electrode in improving the voltage tolerance and signal fidelity. A CPIT or CIT was
396 connected to the electrical loads (20-2000 Ω resistors as examples) with an AC power source
397 (V_{eff} = 0.6 V). The voltage-drop and power of the electrical loads decreased seriously with the

398 decrease of the AC frequency for the CIT-based circuit (Fig. 4a, 4b, Supplementary Figs. S38

399 and S39), but remain excellently stable and high within a wide AC frequency range of 0.1-

400 1000 for CPIT-based circuit. Then, for a more visualized demonstration, two LEDs with

401 antiparallel polarity were also powered by an AC voltage with a triangular waveform (voltage

402 window: −3 to 3 V) (Fig. 4c, Supplementary Fig. S40 and S41). Overall, the voltage across the

403 LEDs has a nonlinear change with input voltage from 2.3 to 3 V, due to the nonlinear voltage-

404 dependent resistance of LED (Fig. 4c, Supplementary Fig. S41) and the non-negligible

405 electrolyte resistance and interfacial impedance of the ionic conductor. According to the

406 current-voltage curves (Figs. 4d and 4e, Supplementary Fig. S41-S47), the CIT-based circuit

407 showed a scan-rate–dependent curves with significant hysteresis and small current (Fig. 4d),

408 indicating the large capacitive impedance of CIT. By contrast, the CPIT-based circuit showed

409 a voltage-dependent current without obvious hysteresis during the scanning cycles, showing

410 the great convenience for LED illumination control. Meanwhile, the voltages across CPIT were

411 much stable (0.53 V when the input voltage reached 3 V), almost independent of the scanning

412 rate, while the voltage across CIT showed a strong dependence on scanning rate, and increased

413 significantly from 0.58 V at a scan rate of 100 V s^{-1} to 0.72 V at 0.2 V s^{-1} when the input

414 voltage reached 3 V (Supplementary Fig. S41), indicating that a higher voltage was applied to

415 the interface of CIT, unbeneficial to the structural stability of ionic conductors.

Ionotronics with spatial-resolved current densities

417   By taking advantage of the ability of the CP hydrogel in tuning local interfacial impedance,

418 a new soft ionotronic model with the controlled spatial distribution of current density was also

419 demonstrated, which will be highly useful for realizing multi-point selective electrical

420 stimulation with a simple device configuration in neuromulation applications, for example.

421 Here, an exemplary ionotronics model was fabricated by coating a polyacrylic acid (PAAc)

422 hydrogel ionic conductor with patterned CP$_{18M}$ hydrogels (Fig. 4f). For measurements, the ionic

423 conductor was divided into nine sections connected in parallel to an AC power source, and then

424 the current through each was measured in real-time. The spatial distribution of current density

425 can be controlled by the presence (or absence) of the CP hydrogel (Figs. 4g and 4h). As shown

426 in the time-dependent current profiles, upon AC power of 10 Hz, the current densities of the

427 sections with four pieces of CP$_{18M}$ larger current were calculated to be ~25 mA cm^{-2}, slightly

428 higher than those with two pieces (~16 mA cm^{-2}). By contrast, the section without CP hydrogel

429 showed only ~10% of the current density of the sections with four pieces. This demonstrated
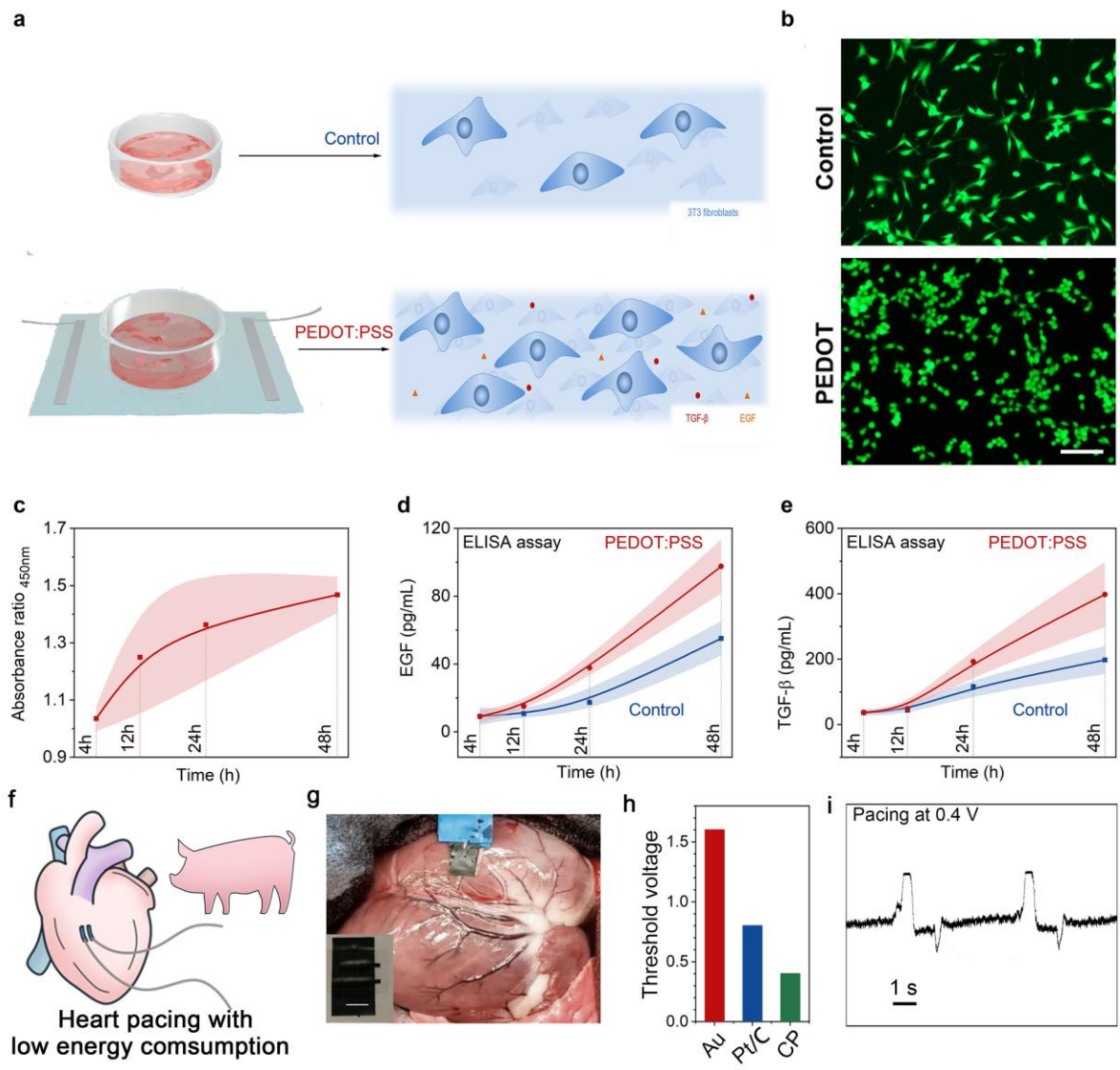
Fig. 5| Biocompatibility of the CP hydrogel. a, Schematics of fibroblasts cultured on a PDMS substrate (control) or a PDMS-supported CP hydrogel substrate with electrical stimulation (CP/electrical stimulation). **b,** LIVE/DEAD staining of fibroblast cells (Scale bar = 100μm). An obvious increase in cell confluency in the experimental group was observed. **c,** Absorbance ratio of cells in CP/electrical stimulation group to those in the control group at 450 nm by CCK-8 assay. **d, e,** ELISA assay analyses of EGF (**d**) and TGF-β (**e**) expression concentration from cell culture supernatant as the function of cell treatment time, with (red) or without (control, blue) CP/electrical stimulation. Two-way ANOVA was used for statistical analysis. *$p < 0.05$, **$p < 0.01$. The shaded regions in panels **c-e** represent standard deviations calculated from three measurements. **f**, **g**, an illustrative schematics and digital photograph of the CP electrodes for heart pacing and porcine heart attached with CP electrodes. **h**, Comparison of the threshold voltage for heart pacing by using different electrodes. **i**, ECG signal recorded during pacing, and schematics of the ECG lead placement.

444   that having the CP_{18M} on a hydrogel ionic conductor could effectively boost the current pass

445   through this region, with respect to the regions not covered by CP (Supplementary Figs. S48

446   and S49). Furthermore, when the AC power frequency decreased down to 1 Hz, the current

447   density of the section without CP hydrogel reduced seriously by more than 50%, reaching only

448   5% of the current relative to that of the section with 4 pieces of CP hydrogel (~21 mA cm^{-2})

449   (Fig. 4g and 4h, Supplementary Fig. 50). Additionally, all the sections with CP_{18M} showed a

450   sinusoidal-shaped waveform, but irregular shapes were observed for sections in absence of

451   CP_{18M}, as the result of severe interference of electrochemical reactions occurring within the

452   metal/electrolyte interfaces, consistent with the previous impedance results. This ionic

453   conductor is also stretchable (Fig. 4i, Supplementary Fig. S51). The CP_{18M} positions in the

454   simulation result (the interfaces were assumed bonded without detachment) showed a good

455   agreement with the experiment, indicating the device integrity could be maintained even after

456   stretching, owing to the excellent adhesiveness of the PAAc hydrogel. Overall, ionic

457   conductors with spatial-resolved current densities can be fabricated through patterning CP

458   hydrogel on the surface of ionic conductors, providing a new ionotronic model for multiplexed

459   sensors and spatial-resolved neural stimulators with soft, stretchable, and partially transparent

460   properties.

461

462 Biocompatibility, benefits in cell proliferation and heart pacing

463   Considering the promising applications of soft ionic-conductor-based devices in

464   bioelectronics and the good biocompatibility of CP hydrogel as reported previously, the

465   biological function of CP hydrogel was studied by taking advantage of its excellent

466   conductivity. Electrical stimulations have been studied and employed as a strategy for

467   therapeutic function in clinical usage recently, including wound healing treatment, neuron

468   regeneration, and infracted myocardium repair[33]. To assess the therapeutic function of our CP

469   hydrogel, fibroblast cells, which played an essential role in the wound healing process, were

470   incubated on our semi-transparent CP hydrogel membrane, and their behavior with electrical

471   stimulation applied was *in vitro* studied (Fig. 5a). Compared with the control group, the

472   fibroblast cells in the group of culturing with CP hydrogel membrane with electric fields had

473   much higher cell confluency (Fig. 5b). Moreover, the LIVE/DEAD staining results showed

474   that most of the cells were alive (green), revealing the good biocompatibility of our CP

475   hydrogel membrane. Noteworthy, many cells stayed round on PEDOT:PSS hydrogel after 48

476   h culturing, suggesting that our CP hydrogel membrane was non-adherent. Such a merit was

477 vital for clinical usage to develop easy-detachable devices, such as wound dressing and
478 temporary implantable scaffolds.[48,49] Furthermore, the cell viability and proliferation after
479 applying electric stimulation were measured by a CCK-8 assay. The cell viability reached the
480 highest percentage after 48 has $146.8\% \pm 4.27\%$ (n=3). The positive correlation of cell viability
481 ratio with time represented in Fig. 5c demonstrated the electric field function in facilitating
482 fibroblast cell proliferation.

483 To further understand the detailed mechanism and the role of electric stimulation through
484 CP hydrogel in promoting cell proliferation, the alternation of growth factor expression in
485 experimental groups was explored by collecting cell culturing supernatant at 4, 12, 24, and 48
486 h, respectively. As a result, the epidermal growth factor (EGF) and transforming growth factor-
487 beta (TGF-β) (Fig. 5d and e), two important growth factors involved in regulating wound
488 healing, showed elevated expression in cells cultured with CP hydrogel with statistical
489 significance (p=0.0099 and 0.0268 respectively). Such an enhanced expression suggested that
490 the increased cell proliferation induced by CP hydrogel could be mapped to growth factors and
491 cellular metabolism pathways, providing a new approach to regulating cell proliferation,
492 assisting wound treatment, and even potentially serving as scaffolds for promoting tissue
493 regeneration by CP hydrogels.

494 Ultimately, to prove the practical applicability and advantages of the CP hydrogel in
495 bioelectronics as a better live tissue-electronic interface, a pair of CP electrodes with exposed
496 areas of ~ 4 mm^2 were fabricated as epicardial electrodes to pace an euthanized porcine heart
497 (Fig. 5f-h). If using commercial metal electrodes and porous Pt/C electrodes, for comparison,
498 the pacing voltage thresholds for Au and Pt/C electrodes were 1.6 V and 1.0 V respectively. By
499 contrast, the CP electrode could stimulate the heart response at a much lower voltage of 0.4 V,
500 due to its strong electron injection ability. Such a significant stimulating power reduction for
501 60-75% presented the great promise of CP electrodes for a pacemaker operating with ultra-low
502 energy consumption. The successful pacing was further validated through the recording of
503 electrocardiogram traces (Fig. 5i).

Conclusion and prospect

505 This work introduced a general strategy of preparing and utilizing ultrastrong, highly
506 conductive and capacitive CP hydrogel electrodes, to solve electron-ion transduction issues,
507 including signal loss and distortion and poor voltage tolerance, which are suffered by nearly
508 all electronics when interfacing with biological tissues or ionic conductors. Attributed to the

19

509 highly-oriented nanoporous structures in the CP hydrogel realized by a gelation-densification

510 strategy, these transduction issues were successfully remedied, enabling better interfacial

511 stability and long-term operation without significant faradic electrochemical processes.

512 Furthermore, by taking advantage of the magnificent difference between CPIT and CIT, an

513 ionic conductor with current density spatial modulation was for the first time demonstrated,

514 providing a new design strategy of spatial-resolved ionic conductors for new functions of

515 ionotronics (*e.g.*, multipoint stimulation by a single probe). Additionally, the great promotion

516 of biological cell proliferation by electrical stimulation and significantly lower voltage

517 threshold of heart pacing using the CP epicardial electrodes, presented not only the advantages

518 in bioelectronics applications with direct tissue contact (*e.g.*, tissue healing and neuron

519 regenerations), and also the strong ion-injection ability. Solving this critical issue makes a step

520 forward for ionotronics and bioelectronics to better bridge the electronic realm with the

521 biological world expectedly, with great promise in transforming human-machine interactions,

522 energy harvesting, sensing, *etc*.

523 Besides the hydrogel-based ionotronics, this CPIT strategy is also expected to be

524 applicable for other subsets of ionic conductors (such as ionic liquids or polyelectrolyte-based

525 ionotronics). The simplicity of this design by using a polymer film electrode allows for

526 combining other functional soft materials, such as bioadhesion. Moreover, considering the high

527 conductivity,   easy   fabrication,   and   outstanding   performance   on   reducing   the

528 electrode/electrolyte interfacial impedance, the CP hydrogels can be directly employed to

529 replace metal to fabricate various ionotronics for much better performance, such as improving

530 the rectifying performance of ionic-based transistors, the output performance of triboelectric

531 generators, and the signal-noise ratio of neural probes.

532 **Methods**

533 **Surface gelation and patterning of CP**. Typically, polydimethylsiloxane (PDMS, Sylgard 184 silicone

534 elastomer, Dow) plates were coated with a layer of Fe_{mp} of 1-3 μm (40337 iron powder, spherical, Alfa

535 Aesar) by spray-coating 50 mg mL^{-1} Fe_{mp} isopropanol solution (Supplementary Fig. S3). Subsequently, 6

536 mL of pristine PDEOT:PSS suspension (11-13 mg mL^{-1}, Celvios PH1000, Heraeus) was dropped onto

537 PDMS substrate (5.4×5.4 cm^2) and kept static for 12 h. Finally, CP hydrogel on PDMS was obtained after

538 etching residual Fe_{mp} by 0.5 M H_2SO_4. CP hydrogel with a low or high loading was also prepared by using

539 the 3.5 mL or 8.3 mL of pristine CP suspension as the precursor.

540 For the patterning of CP hydrogel, Fe_{mp}-coated PDMS was attached with a mask (Magic tape, Scotch) with

541 a designed pattern (fabricated by laser cutting (LS-3655, Bosslaser)). 3 mg mL^{-1} CP suspension was dropped

542 onto the substrate and kept still for 20 min. Finally, CP hydrogel with patterns was obtained after removal

543 of the mask and etching the residual Fe_{mp} by 0.5 M H_2SO_4.

544

545 **Preparations of the free-standing CP hydrogel.** The as-prepared CP hydrogel on the PDMS substrate was

546 chemically treated by H_2SO_4 solution with a gradient concentration from 1 mol L^{-1} to 12 mol L^{-1}. Then, the

547 free-standing CP_{12M} was obtained after the dialysis in purified water for 2 days to remove H_2SO_4. The CP_{18M}

548 was obtained by further treating free-standing CP_{12M} with concentrated H_2SO_4, followed by dialysis for 2

549 days. $CP_{D20\%}$, $CP_{D10\%}$, and $CP_{D5\%}$ were densified CP_{18M}, which were prepared by exchanging water in CP_{18M}

550 with H_2SO_4 solution of different concentrations (volumetric ratio of H_2SO_4 and water = 20%, 10%, and 5%,

551 respectively), followed by drying at 70 ^oC for 2 h and dialysis in water for 2 days.

552

553 **Preparations of optically transparent CP hydrogel membrane.** 1.5 mg mL^{-1} CP suspension was dropped

554 onto a Fe_{mp}-coated PDMS substrate and kept static for 30 s to 5 min, followed by chemical treatment by

555 H_2SO_4 solution with gradient concentration from 1 mol L^{-1} to 12 mol L^{-1}. Finally, transparent CP hydrogel

556 membranes supported by a PDMS substrate was obtained after dialysis for 12 h. The optically transparent

557 CP hydrogel are beneficial for observation, and thus were used for the cell culturing studies.

558

559 **Fabrication of ionic conductors.** Typically, without particular notice, a PVA hydrogel (length, width, and

560 thickness is 4 cm, 1.1 cm, and 0.4 cm, respectively) was employed as a matrix and was infiltrated with

561 different electrolytes (1 M H_2SO_4, or 3, 1, 0.5, or 0.154 M NaCl solution) to fabricate ionic conductor, which

562 was attached with two pieces of Pt plates (0.9×0.9 cm^2) for CIT or CP_{18M} hydrogels (0.9×0.9 cm^2) for CPIT

563 at its two ends. Finally, the ionic conductor was connected to external circuits through Pt leads for tests.

564 Noteworthy, the PVA hydrogel had shrinkage in the size when NaCl solution with high concentration was

565 infiltrated (the size of PVA changed into 2.7×0.95×0.35 cm^3). Besides, for the generality study of CPITs,

566 PVA hydrogel strip with the same width (1.1 cm) and thickness (0.4 cm) but with different lengths (6.4 cm

567 and 14 cm) were also employed as matrix and was infiltrated with 3M NaCl electrolytes to fabricate ionic

568 conductor. Hydrogels from different polymers (PAAc, poly(N-isopropylacrylamide), polyacrylamide) were

569 also prepared, infiltrated with 3 M NaCl electrolyte, and finally cut into a similar size of ~ 2.7×0.95×0.35

570 cm^3 to fabricate ionic conductors.

571

572 **Characterizations of structure:** SEM micrographs were taken out on a field emission scanning electron

573 microscope (Supra 40VP, ZEISS). XPS was obtained using an X-ray photoelectron spectrometer (Axis Ultra,

574 Kratos) with an exciting line of Al Kα. Raman spectra were recorded by a confocal Raman microscope upon

575 the laser of 633 nm (inVia Inspect, Renishaw). Ultraviolet-visible (UV-vis) spectra were recorded by UV-

576 vis spectrometer (UV-3101PC, Shimadzu).

577

578   **Electrical conduction measurement.** For CP_{12M}, CP_{18M}, and its densified counterparts, conductivity was
579   measured by using a four-point probe head with tungsten carbide electrodes (C4S probe, Cascade
580   Corporation) coupled with a digital multimeter (4200 digital multimeters, Keithley). The CP hydrogel was
581   cut into a square shape of 3×3 cm^2, and its conductivity (σ) was calculated by Eq. 3.

582   $$\sigma = \frac{I}{4.53 \times V \times T} \qquad (Eq.\,3)$$

583   , where I, V, and T are current, voltage, and thickness of the CP hydrogel, respectively.

584   For transparent CP hydrogels supported by PDMS substrates, the sheet resistance (R_s) was measured
585   by using the CP hydrogel with a rectangular shape of 3×1 cm^2, through the AC impedance method in a two-
586   electrode configuration on an electrochemical working station (CHI660E, CH Instrument) with the
587   amplitude of 5 mV. To avoid the dehydration of CP hydrogel, purified water was dropped onto the CP
588   hydrogel. The sheet resistances of CP hydrogel were calculated by Eq. 4, and were fitted against the optical
589   transmittance at 418 nm by Eq. 5.

590   $$R_s(\omega) = \frac{|Z(\omega)| \times W}{L} \qquad (Eq.\,4)$$

591   , where $|Z(\omega)|$ is the modulus of impedance, L is the distance between two electrodes, W is the width of CP
592   hydrogel.

593   $$T = \left(1 + \frac{Z_0}{2R_s}\frac{\sigma_{op}}{\sigma_{dc}}\right)^{-2} \qquad (Eq.\,5)$$

594   , where T is the transmittance, Z_0 is the impedance of free space (377 Ω), Rs is the sheet resistance, σ_{op} and
595   σ_{dc} are the optical and electrical conductivities respectively. According to the fitting results, σ_{op}/σ_{dc} is
596   calculated to be ~20.

597

598   **Mechanical measurements.** PEDOT:PSS hydrogels were cut into a rectangular shape with a width of 1 cm^2,
599   and its tensile strain-stress curves were recorded on a dynamic mechanical analyzer (DMA850, TA
600   instruments) in a tensile mode at the strain rate of 100 % strain per minute (gauge length = 3 cm). Before the
601   tests, the hydrogels were spray-coated with enough water to avoid the dehydration of the PEDOT:PSS
602   hydrogel.

603

604   **Electrochemical characterizations in a three-electrode system.** Three-electrode system was employed to
605   study the intrinsic electrochemical properties of the PEDOT:PSS hydrogel through an electrochemical
606   working station (CHI660E, CH Instrument). Free-standing PEDOT:PSS hydrogel (0.9$\times$0.9 cm^2), Pd/Au
607   plate (3$\times$1 cm^2), SCE were employed as working, counter, and reference electrodes, respectively. 0.1 mol
608   L^{-1} H$_2$SO$_4$ or NaCl of different concentrations (3, 1, 0.5, or 0.154 mol L^{-1}) was employed as an electrolyte.
609   In CV and GCD measurements, the electrochemical windows were controlled to be 0-0.8 V (vs. Hg/Hg$_2$Cl$_2$)
610   for all these electrolytes except 3 mol L^{-1} NaCl electrolyte (0-0.7 V). EIS spectra were obtained at an initial
611   potential of 0 V (vs. SCE) with 5 mV amplitude in the frequency range of 10^5-0.025 Hz. The areal

612   capacitance (C_A), specific volumetric capacitance (C_V), IR drop (V_{IR}), and coulombic efficiency (CE) were

613   calculated by Eqs. 6-9 respectively.

614
$$C_A = \frac{I \times t_{cathodic}}{A \times E_{high}} \qquad \text{(Eq. 6)}$$

615
$$C_A = \frac{I \times t_{cathodic}}{V \times E_{high}} \qquad \text{(Eq. 7)}$$

616
$$V_{IR} = E_{high} - E_{ini} \qquad \text{(Eq. 8)}$$

617
$$CE = \frac{t_{cathodic}}{t_{anodic}} \qquad \text{(Eq. 9)}$$

618   , where I is cathodic or anodic current, $t_{cathodic}$ and t_{anodic} are cathodic and anodic time respectively, E_{max} and

619   E_{ini} are the high potential limit and the potential at the beginning of the cathodic process, respectively, and

620   A and v are the area and volume of the working electrode.

621   The areal real capacitance (C') and resistor-capacitor time constant (τ_{RC}) derived from EIS spectra were

622   calculated by Eqs. 10 and 11.

623
$$C'(\omega) = \frac{-Z''(\omega)}{A \times \omega \times |Z(\omega)|^2} \qquad \text{(Eq. 10)}$$

624
$$t_{RC} = Z'(\omega) \times \frac{-Z''(\omega)}{A \times \omega \times |Z(\omega)|^2} \qquad \text{(Eq. 11)}$$

625    $|Z(\omega)|$ is the modulus of impedance, $Z'(\omega)$, $Z''(\omega)$ are real and imaginary parts of impedance, A is areal of

626   working electrodes, and ω is the angular frequency.

627

628   **Impedance test and analysis of ionic conductors.** Except for particular notice, the impedances of CIT and

629   CPIT were recorded by an electrochemical working station (CHI660E, CH Instrument) at the voltage of 0 V

630   with an amplitude of 5 mV from 10^5 to 0.02 Hz. The CIT and CPIT were connected to the electrochemical

631   working station by Pt wire. The diffusion resistances were obtained from EIS spectra according to the

632   electrochemical model (See Supplementary Discussion Section 4 for details).

633

634   **Electric measurement of ionotronics loaded with resistors or LED.** For ionotronics loaded with a resistor,

635   a CIT or CPIT was fabricated as ionotronic devices by employing a PVA hydrogel ($2.7 \times 0.95 \times 0.35$ cm^3) as

636   polymer matrixes, 3 M NaCl solution as electrolytes, and two CP$_{18M}$ hydrogels (0.9×0.9 cm^2, areal

637   capacitance ~110 F cm^{-2} at 0.62 mA cm^{-2}) for CPITs or Pt plate (0.9×0.4 cm^2) for CITs as electrodes. Upon

638   an AC power, the voltages across the resistors were calculated from the measured currents by the Ohm's

639   Law.

640   For ionotronics loaded with LEDs, A CIT or CPIT was fabricated by employing a PVA hydrogel (length: 7

641   cm, width: 1.2 cm, thickness 0.4 cm) as polymer matrixes, 3 M NaCl as electrolytes, and two CP$_{18M}$

642   hydrogels (0.9×0.4 cm^2, areal capacitance ~110 F cm^{-2} at 0.62 mA cm^{-2}) or Pt plate (0.9×0.4 cm^2) as

643   electrodes. Then, Two LEDs with antiparallel polarity were connected to an electrochemical working station

644   (as AC power source and current meter) through a CIT or CPIT, which was then powered by an AC voltage

645   with a triangular waveform (voltage window: −3 to 3 V). The voltage across the LEDs and the ionic

646   conductor were recorded by a digital multimeter (4200 digital multimeters, Keithley) in real-time.

647

648   **Ionic conductors with spatial-resolved current densities.** Adhensive PAAc-hydrogel-based ionic

649   conductor was prepared after 8 g acrylic acid, 15 mg bis, 30 mg VA-044 were added into 32 mL of water,

650   kept still at 60°C for 30 min, and infiltrated with 3 M NaCl solutions. Then, CP_{18M} hydrogels were cut into

651   a rectangular shape of ~0.2×0.2 cm^2 and attached to the surface of PAAc hydrogel directly. For the current

652   density test, the ionic conductor was divided into 9 domains (9.3×9.3 mm^2), and all these domains acted as

653   top electrodes connected in parallel through Pt plates, while another CP_{18M} hydrogel adhered on the other

654   side of PAAc hydrogel acted as the bottom electrodes. Top and bottom electrodes were connected to an

655   electrochemical working station as an AC power source and applied by an input AC voltage (V = 0.848 sin

656    $(2\pi f t)$ where f = 1 or 10 Hz). The currents passing through each domain were recorded in real-time by a

657   digital multimeter (4200 digital multimeters, Keithley).

658

659   **Mechanical Simulation of the ionotronics with spatial-resolved current densities.**   The simulation was

660   done using SolidWorks®. The mechanical property of the PAAc hydrogel was measured using DMA 850

661   (Texas Instruments) and was used as the input for the simulation. The mechanical property of the CP_{18M}

662   hydrogel previously mentioned in this work was used. The bonding between CP_{18M} and PAAc hydrogel was

663   set as bonded to represent a non-slip attachment. Two additional blocks with extremely high modulus are

664   introduced to the model and set to bond with the PAAc, to ensure that the two ends of the hydrogel are

665   stretched homogeneously. To ensure an acceptable simulation time and satisfactory accuracy, we set the

666   mesh to be denser around the PEDOT and sparser at other areas. The non-linear simulation was run with the

667   final state of the PAAc to have the same length as in the experiment.

668

669   **Cell culture and electric stimulation.** NIH 3T3 fibroblast cells were cultured in Dulbecco's modified

670   Eagle's medium (Thermofisher Scientific) supplemented with 10% bovine serum (Thermofisher Scientific)

671   in PDMS molds with the size of 5×1 mm^2. For control groups, cells were directly cultured on Petri dishes.

672   For experimental groups, cells were cultured directly on CP-coated PDMS connected to Arbitrary Function

673   Generator (AFG1000, Tektronix Inc.) by gold electrodes. The parameter for electric stimulation (verified

674   with an oscilloscope) was set up as 2Hz, 1.2 V/mm with 1ms pulse width according to the previous studies.[45]

675   All devices for cell culture were sterilized by UV light for 20 min.

676

677   **Cell viability test.** To assess cell viability after being treated with or without PEDOT:PSS for 48 h, cells

678   were stained by using LIVE/DEAD cell staining kit (Thermofisher Scientific), washed with DPBS twice,

679   and then evaluated by microscope (Zeiss Axio observer, Zeiss). To test cell proliferation, after 10% CCK-8

680   was added in each well and incubated for 2 h at 37 °C, the absorbance at 450 nm was measured by a plate

681   reader (n=3) (SpectraMax M5, Molecular Devices). The growth factors secreted by fibroblast cells were

682   tested by EGF and TGF-β ELISA assay kit (Thermofisher Scientific). Briefly, the supernatant of cell culture

683   mediums was collected for each well at 4, 12, 24, 48 h after seeding of cells and electric stimulation, and

684   were analyzed by a microplate reader (SpectraMax M5, Molecular Devices).

685

686   ***Ex vivo ventricular pacing***. A postmortem study was performed in a male Yucatan miniature pig (S & S

687   Farms, Ranchita, Calif). All animal studies were approved by the UCLA Office of Animal Research in

688   compliance with the UCLA IACUC protocols. The porcine epicardium was exposed through thoracotomy

689   conducted by an experienced veterinarian from the UCLA Department of Animal and Laboratory Medicine.

690   Then, the CP electrodes with an exposed areal of 4 mm^2 were attached onto the epicardium of the right

691   ventricles. Immediately after euthanasia, external pacing with an amplitude of 2 V, pulse width of 1 ms at

692   the rate of 60 beat per minutes was initiated according to previous literature[34], while a simultaneous

693   electrocardiogram (ECG) was recorded for monitoring cardiac rhythm and assessing pacemaker

694   effectiveness.

695

696

697   **Data availability.** The data that support the plots within this paper and other findings of this study are

698   available from the corresponding authors on request.

699

700

701

705

706   **Author contributions**

707   B.Y. and X.H. designed research; B.Y., Y.Y., and C.W. performed experimental research; S.D.

708   performed the mechanical analysis of ionic conductor; D.W. and Y.Z. contributed new reagents and

709   analytic tools; B.Y., Y.Y. and X.H. analyzed data; and B.Y., Y.Y., X.Z., and X.H. wrote the paper.

710

711   **Additional information**

712   Supplementary information is available for this paper.

713

714   **Competing interests**

715   The authors declare no competing financial interests.

716

Reference

1. Yang, C. & Suo, Z. Hydrogel ionotronics. *Nat. Rev. Mater.* **3**, 125-142 (2018).
2. Kim, D.H. et al. Materials for multifunctional balloon catheters with capabilities in cardiac electrophysiological mapping and ablation therapy. *Nat. Mater.* **10**, 316-323 (2011).
3. Wise, K.D., Anderson, D.J., Hetke, J.F., Kipke, D.R. & Najafi, K. Wireless Implantable Microsystems: High-Density Electronic Interfaces to the Nervous System. *Proceedings of the IEEE* **92**, 76-97 (2004).
4. Boehler, C., Carli, S., Fadiga, L., Stieglitz, T. & Asplund, M. Tutorial: guidelines for standardized performance tests for electrodes intended for neural interfaces and bioelectronics. *Nat. Protoc.* **15**, 3557-3578 (2020).
5. Song, E., Li, J., Won, S.M., Bai, W. & Rogers, J.A. Materials for flexible bioelectronic systems as chronic neural interfaces. *Nat. Mater.* **19**, 590-603 (2020).
6. Climbing-inspired twining electrodes using shape memory for peripheral nerve stimulation and recording. *Sci. Adv.* **5**, eaaw1066 (2019).
7. Fang, Y. et al. Micelle-enabled self-assembly of porous and monolithic carbon membranes for bioelectronic interfaces. *Nat. Nanotechnol.* **16**, 206-213 (2021).
8. Chun, J. et al. Boosted output performance of triboelectric nanogenerator via electric double layer effect. *Nat. Commun.* **7**, 12985 (2016).
9. Schroeder, T.B.H. et al. An electric-eel-inspired soft power source from stacked hydrogels. *Nature* **552**, 214-218 (2017).
10. Zou, Y. et al. A bionic stretchable nanogenerator for underwater sensing and energy harvesting. *Nat. Commun.* **10**, 2695 (2019).
11. Kim, B. et al. Robust High Thermoelectric Harvesting Under a Self-Humidifying Bilayer of Metal Organic Framework and Hydrogel Layer. *Adv. Funct. Mater.* **29**, 1807549 (2019).
12. Tybrandt, K., Forchheimer, R. & Berggren, M. Logic gates based on ion transistors. *Nat. Commun.* **3**, 871 (2012).
13. Tybrandt, K., Larsson, K.C., Richter-Dahlfors, A. & Berggren, M. Ion bipolar junction transistors. *Proc. Natl. Acad. Sci. U.S.A.* **107**, 9929-9932 (2010).
14. Yang, C.H., Chen, B., Zhou, J., Chen, Y.M. & Suo, Z. Electroluminescence of Giant Stretchability. *Adv. Mater.* **28**, 4480-4484 (2016).
15. Liu, X., Liu, J., Lin, S. & Zhao, X. Hydrogel machines. *Mater. Today* **36**, 102-104 (2020).
16. Li, T.F. et al. Fast-moving soft electronic fish. *Sci. Adv.* **3**, e1602045 (2017).
17. Zhu, B., Gong, S. & Cheng, W. Softening gold for elastronics. *Chem. Soc. Rev.* **48**, 1668-1711 (2019).
18. Son, D. et al. Multifunctional wearable devices for diagnosis and therapy of movement disorders. *Nat. Nanotechnol.* **9**, 397-404 (2014).
19. Keplinger, C. et al. Stretchable, Transparent, Ionic Conductors. *Science* **341**, 984 (2013).
20. Liu, J. et al. Intrinsically stretchable electrode array enabled in vivo electrophysiological mapping of atrial fibrillation at cellular resolution. *Proc. Natl. Acad. Sci. U.S.A.* **117**, 14769-14778 (2020).
21. Yu, Y., Nyein, H.Y.Y., Gao, W. & Javey, A. Flexible Electrochemical Bioelectronics: The Rise of In Situ Bioanalysis. *Adv. Mater.* **32**, e1902083 (2020).
22. Hong, G. & Lieber, C.M. Novel electrode technologies for neural recordings. *Nat. Rev. Neurosci.* **20**, 330-345 (2019).
23. Li, Z. et al. Tuning the interlayer spacing of graphene laminate films for efficient pore utilization towards compact capacitive energy storage. *Nat. Energy* **5**, 160-168 (2020).
24. Yang, X., Cheng, C., Wang, Y., Qiu, L. & Li, D. Liquid-Mediated Dense Integration of Graphene Materials for Compact Capacitive Energy Storage. *Science* **341**, 534-537 (2013).
25. Sheberla, D. et al. Conductive MOF electrodes for stable supercapacitors with high areal capacitance. *Nat. Mater.* **16**, 220-224 (2017).

768   26.   Yao, B. et al. Ultrahigh-Conductivity Polymer Hydrogels with Arbitrary Structures. *Adv. Mater.*
769   **29**, 1700974 (2017).

770   27.   Feig, V.R. et al. An Electrochemical Gelation Method for Patterning Conductive PEDOT:PSS
771   Hydrogels. *Adv. Mater.*, e1902869 (2019).

772   28.   Lu, B. et al. Pure PEDOT:PSS hydrogels. *Nat. Commun.* **10**, 1043 (2019).

773   29.   Zhang, S.M. et al. Room-Temperature-Formed PEDOT:PSS Hydrogels Enable Injectable, Soft,
774   and Healable Organic Bioelectronics. *Adv. Mater.* **32**, 7 (2020).

775   30.   Govindarajan, A.V., Je, M., Park, W.T. & Achyuta, A.K.H. in MEMS for Biomedical
776   Applications. (eds. S. Bhansali & A. Vasudev) 361-395 (Woodhead Publishing, 2012).

777   31.   Chen, G. et al. Strain- and Strain-Rate-Invariant Conductance in a Stretchable and
778   Compressible 3D Conducting Polymer Foam. *Matter* **1**, 205-218 (2019).

779   32.   Xia, Y.J., Sun, K. & Ouyang, J.Y. Solution-processed metallic conducting polymer films as
780   transparent electrode of optoelectronic devices. *Adv. Mater.* **24**, 2436-2440 (2012).

781   33.   Nunes, S.S. et al. Biowire: a platform for maturation of human pluripotent stem cell-derived
782   cardiomyocytes. *Nat. Methods* **10**, 781-787 (2013).

783   34.   Abiri, P. et al. Inductively powered wireless pacing via a miniature pacemaker and remote
784   stimulation control system. *Sci Rep.* **7**, 6180 (2017).

785

Supplementary Files

This is a list of supplementary files associated with this preprint. Click to download.

- SIfinal.docx